

Evaluation of Polarimetric Eigenvector Based Decomposition for Types of Wetland Mapping

Ruma Adhikari (✉ radhikari@ce.iitr.ac.in)

IIT Roorkee: Indian Institute of Technology Roorkee <https://orcid.org/0000-0003-2966-3302>

Short Report

Keywords: Polarimetric SAR, Polarimetric decomposition, Herbaceous wetland, Aluvial fan

Posted Date: June 14th, 2021

DOI: <https://doi.org/10.21203/rs.3.rs-581046/v1>

License:  This work is licensed under a Creative Commons Attribution 4.0 International License.

[Read Full License](#)

1 **Title**

2

3 **Evaluation of Polarimetric Eigenvector Based**
4 **Decomposition for Types of Wetland Mapping**

5

6 Author: Ruma Adhikari

7 Affiliation: Department of Geomatics Engineering, Indian Institute of

8 Technology Roorkee, P.O.- IIT Roorkee, District- Haridwar, Uttarakhand,

9 India, 247667

10 Email: radhikari@ce.iitr.ac.in, adhikari.ruma12@gmail.com

11 Phone: +91-8017139744

12 ORCID ID: [0000-0003-2966-3302](https://orcid.org/0000-0003-2966-3302)

13

14

15

16

17

18

19

20

21

22

23

24

25

26 **Abstract**

27 **Context**

28 The Kosi mega fan landscape is an alluvial deposited site that have led to several devastating floods. A
29 considerable portion of the land comprises of different types of wetlands and persistent surface wetness.
30 Detection of these wet patches is important in terms of understanding morphology of this sediment
31 deposited fan.

32 **Objectives**

33 This study identifies different wetland patches in monsoon time with critical reaches of rail-road and
34 waterlogged intersections.

35 **Methods**

36 SAR Polarimetry based H-A-Alpha decomposition and Wishart classification is used to identify different
37 backscatter intensities of vegetated wetland, wet soil and open water using dual-pol Sentinel-1 10m data.

38 **Results**

39 This study showed that Wishart classification offers a good potential for herbaceous waterbody mapping.
40 The presence of a varieties types of wetlands is identified based on their scattering properties. Preliminary
41 it has identified wet soil, low land, marshy patches as well as open water. Though at some places it
42 mistakenly classified vegetation covered water as forest land. Some dry soil also exhibits low entropy
43 volume scattering which is similar to certain type of vegetation cover. This study also identifies the
44 vulnerable zone of waterlogging to existing rail and road network.

45 **Keywords:** Polarimetric SAR, Polarimetric decomposition, Herbaceous wetland, Aluvial fan

46 **1. Introduction**

47 Waterlogging occurs due to saturation of ground with water. It can be a combination of factors like poor
48 drainage, improper infiltration, excess rainfall, ground water level or anthropogenic activities. Waterlogged
49 patches can be found in areas of saturated ground water. During monsoon the landform comprises of
50 floodwater, herbaceous and hyacinth wetlands.

51 Kosi delta is the ecological and socio-economic hub of the state Bihar. The delta is a source of
52 multiple ecosystem services critical to ecological and economic security of the region.

53 Remote sensing can be defined as the acquisition of information about an object or phenomenon
54 without making physical contact with the target. Observations in visible spectrum are being used for several
55 decades but are limited in certain prospects like dependency on sun energy, weather etc. The active
56 microwave remote sensing is both time and weather independent, penetration of earth surface cover is
57 higher compared to optical region.

58 A SAR system illuminates earth surface with continuous strips of signal and records back the
59 receiving signal towards radar sensor. The radar antenna records the strength and time delay of return
60 signals. SAR polarimetry measures the polarimetric properties of man-made and natural scatterers. The
61 backscattering is sensitive to shape, reflectivity, orientation and geophysical properties of the targeted
62 scatterers. This scattering information is stored in the form of “scattering matrix”.

63 It can be defined as an approach to extract and parameterising the target information from
64 backscatter of a single-look POLSAR data; same as coherency matrix for multi-look data. The polarimetric
65 decomposition method can be defined as aims on separating the polarimetric measurement from a random
66 media into independent elements which can be associated to the various physical scattering mechanism on
67 ground (Boerner, n.d.)

68 Based on transmitting and receiving signal, polarized signals can be described as three types:

- 69
- Single polarized (either HH or VV or HV or VH)

- 70 • Dual polarized (HH and VV) or (HH and HV) or (HV and VV)
- 71 • Quad or fully polarized (HH, VV, HV, VH)

72 2. Literature background

73 According to (Zhang et al. 2016) C-band is more useful for low density herbaceous wetlands. An approach
 74 for dual-polarised data is performed using Kennaugh matrix (Moser et al. 2016). Quad pol TerraSAR-X
 75 has its proven accuracy in extracting wetland vegetation types (Hong et al. 2015). One of the eigenvector
 76 based decompositions is the H-A- α or Shannon entropy, which can cope with dual-polarised data (Lee and
 77 Pottier 2017).

78 The use of SAR Polarimetry in flood mapping with its backscatter and coherence feature started
 79 in 2003 (Van Zyl and Kim 2003). The development of Polarimetric sar started in 1940^s with Sinclair,
 80 Kennaugh and Huynen matrix parameters later followed by Ulaby and Fung (Xiang 2016). In (ZYL, n.d.)
 81 Van Zyl experimented with Eigenvector based algorithms to get all the information of scattered wave in
 82 vector measurement process by using two coherent receiver channels. This provides basis invariant
 83 description of the scatterers in terms of three parameters ie. Entropy, Anisotropy and α -parameter. Wishart
 84 Classification

85 Next, based on the results of the decompositions explained above, an unsupervised Wishart classification
 86 is applied to derive the land cover of the AOI. The Wishart polarimetric classification procedure executes
 87 a Maximum Likelihood (ML) statistical segmentation of a polarimetric data set based on the multivariate
 88 complex Wishart probability density function.

89 The backscatter intensity of pixels-based approach can cause similar intensity for two types of
 90 objects. In this case it cannot differentiate between these two objects. Polarimetric parameter-based
 91 decomposition techniques can overcome this issue by providing different scattering mechanisms.

92 In order to extend the classification scheme and to improve the capability to distinguish different
 93 types of scattering process, it is proposed to use some combinations between entropy(H) and anisotropy(A).
 94 A combined unsupervised classification method that uses the H/ α decomposition and the supervised
 95 Wishart classifier (Lee et al. 1999). The total number of classes are achieved here is 16.

96 For, $A < 1/2$ and $A > 1/2$

97 A1 - The (1-H) (1-A) image corresponds to presence of single dominant scattering process (low
 98 entropy, low anisotropy).

99 A2 - The H(1-A) image says a random scattering process (high entropy, low anisotropy).

100 A3 - The (1-H) A corresponds to the presence of two scatterings with dominant process (low to
 101 medium entropy) and a second one with medium probability (high anisotropy).

102 A4 - The HA image relates to the presence of two scattering mechanisms with same probability
 103 (high entropy, high anisotropy).

104 2.1 Polarimetric Decomposition

105 It can be defined as an approach to extract and parameterising the target information from backscatter.
 106 Aims on separating the polarimetric measurement from a random media into independent elements which
 107 can be associated to the various physical scattering mechanism on ground.

108 For the study an eigen vector-based decomposition is used.

109 2.1.1 Eigenvector-based

110 In linear algebra, an eigenvector or characteristic vector of a linear transformation is a nonzero vector that
 111 changes at most by a scalar factor when that linear transformation is applied to it.

112 If T is a linear transformation from a vector space V over a field F into itself and \mathbf{v} is a vector
 113 in V that is not the zero vector, then \mathbf{v} is an eigenvector of T if $T(\mathbf{v})$ is a scalar multiple of \mathbf{v} .

114 This condition can be written as the equation

$$115 T(v) = \lambda(v)$$

116 where λ is a scalar in the field F , known as the eigenvalue, characteristic value, or characteristic
 117 root associated with the eigenvector v .

118 • **Cloude-Pottier decomposition**

119 The eigenvector-based analysis of the coherency $\langle [T] \rangle$ matrix is used since it provides a basis invariant
 120 description of the scatterers. The eigenvectors represent the scattering process and their relative magnitude
 121 by the eigenvalues. A diagonal form of 3×3 coherency matrix of eigenvalues is generated which can
 122 physically interpret the statistical independence between a set of targets.

123 A coherency matrix can be written as:

$$\langle [T] \rangle = [U_3][\Sigma][U_3]^{-1} \quad (i)$$

124 Where $[\Sigma]$ is a 3×3 diagonal matrix which contains the eigenvalues of T

$$\Sigma = \begin{bmatrix} \lambda_1 & 0 & 0 \\ 0 & \lambda_2 & 0 \\ 0 & 0 & \lambda_3 \end{bmatrix} \quad (ii)$$

125 Such that $\infty > \lambda_1 \geq \lambda_2 \geq \lambda_3 > 0$

126 And

$$[U_3] = [u_1 \quad u_2 \quad u_3] \quad (iii)$$

127 Is a 3×3 unitary matrix where u_1, u_2, u_3 are the three-unit orthogonal eigenvectors. With these
 128 three independent targets a statistical model can be constructed, expansion of $\langle [T] \rangle$ into the sum of these
 129 three uncorrelated targets. Each of the targets represents a single scattering matrix.

130 The decomposition model is as follows:

$$\langle [T] \rangle = \sum_{i=1}^{i=3} \lambda_i [T_i] = \sum_{i=1}^{i=3} \lambda_i u_i u_i^{*T} \quad (iv)$$

132 Where the real numbers λ_i are the eigenvalues of $\langle [T] \rangle$.

133 Cases:

134 If any one of the eigenvalues is non-zero, then the respective coherency matrix $[T_i]$ corresponds
 135 to a pure target and can be related to a single scattering matrix.

136 If the eigenvalues are equal, the $[T_i]$ is of equal amplitudes, and the target is said random.

137 • **Entropy**

138 It is an eigenvalue parameter calculated to find out the statistical disorder of each target by the logarithmic
 139 sum of eigenvalues of $[T_i]$ as follows:

$$H = - \sum_{i=1}^{i=3} P_i \log_3(P_i) \quad (v)$$

140 P_i is the probabilities obtained from eigenvalues.

141 Cases:

142 When H is low, the system may be considered as depolarizing and the matrix corresponding to the largest
 143 eigenvalue is dominant; other eigenvector components can be ignored.

144 When H is high, the full eigenvalue spectrum has to be considered.

145 As the H increases, the number of distinguishable classes is reduced.

146 The H determines the degree of randomness of the scattering process, which can be also interpreted as the
147 degree of statistical disorder. Thus

148 $H \rightarrow 0$

149 $\lambda_1 = \text{SPAN} \qquad \lambda_2 = 0 \qquad \lambda_3 = 0$

150 The scattering process corresponds to a pure target.

151 $H \rightarrow 1$

152 $\lambda_1 = \frac{\text{SPAN}}{3}$

153 $\lambda_2 = \frac{\text{SPAN}}{3}$

154 $\lambda_3 = \frac{\text{SPAN}}{3}$

155 Here rank=3, so the scattering process is due to the combination of three pure targets. Mostly corresponds
156 to volume scattering.

157 • **Anisotropy**

158 Another eigenvalue parameter can be defined as:

$$A = \frac{\lambda_2 - \lambda_3}{\lambda_2 + \lambda_3} \qquad \text{(vi)}$$

159 It is a parameter complimentary to the Entropy. It measures the relative importance of the second and third
160 eigenvalues of the eigen decomposition.

161 Cases:

162 When $A = 0$, $\lambda_2 = \lambda_3$

163 This can happen for a dominant scattering mechanism, when λ_2, λ_3 are close to zero.

164 Or,

165 For the case of a random scattering type where the three eigenvalues are equal.

166 The modulus of the three eigenvectors are directly function of the three Huynen target generators.

167 The nine numbers of Huynen parameters ($A_0, B_0, B, C, D, E, F, G$ and H) are interrelated in such a way as
168 to reflect directly the physical source of correlation effects in the target. Each of these parametrs contains
169 physical target information. Both for the pure target(strong scatterer) and distributed target(natural media),
170 the three diagonal components of coherency matrix ($A_0, B_0 + B, B_0 - B$) are connected as follows:

171 Symmetry $\rightarrow 2A_0 \rightarrow |S_{HH} + S_{VV}| \rightarrow$ Blue

172 Irregularity/ double bounce/ dihedral $\rightarrow B_0 + B \rightarrow |S_{HH} - S_{VV}| \rightarrow$ Red

173 Non-symmetry/ volume $\rightarrow B_0 - B \rightarrow |S_{HV}| \rightarrow$ Green

174 Anisotropic behaviour is commonly predicted for geometric scatterers (scatterers with a simple geometric
175 structure), but it may also arise from volumetric scatterers (random arrangements of interfering point
176 scatterers).

177

178

179

180 • **α -parameter**

181

$$\bar{\alpha} = \sum_{i=1}^3 p_i \alpha_i \quad (\text{vi})$$

182 The interpretation of the scattering mechanisms given by the eigenvectors of the decomposition, u_i for
183 $i=1,2,3$ is performed by means of a mean dominant mechanism which can be defined as follows:

$$u_0 = [\cos \bar{\alpha} \quad \sin \bar{\alpha} \cos \bar{\beta} e^{j\bar{\delta}} \quad \sin \bar{\alpha} \cos \bar{\beta} e^{j\bar{\gamma}}]^T \quad (\text{iii})$$

184 Where the remaining average angles are defined same way as $\bar{\alpha}$

$$\bar{\beta} = \sum_{i=1}^3 p_i \beta_i$$

$$\bar{\delta} = \sum_{i=1}^3 p_i \delta_i$$

$$\bar{\gamma} = \sum_{i=1}^3 p_i \gamma_i$$

188 $\bar{\alpha} \rightarrow 0$: the scattering corresponds to single bounce scattering produced by a rough surface

189 $\bar{\alpha} \rightarrow \frac{\pi}{4}$: the scattering corresponds to volume scattering

190 $\bar{\alpha} \rightarrow \frac{\pi}{2}$: the scattering corresponds to double-bounce scattering

191 The α angle describes the type of backscattering, ranging from very small α values (close to zero) which
192 indicate domination of surface scattering (single bounce scattering), to high α values representing
193 domination of double bounce scattering (e.g., indication of either urban area or tree trunks).

194 α values in between the aforementioned extremes (i.e., $\sim 45^\circ$) show domination of volume
195 scattering, caused by multiple scattering inside a volume, e.g., such as the crown of a tree (dense
196 vegetation).

197 The entropy H represents the heterogeneity of the scattering and ranges from 0, which indicates a
198 dominant scatterer such as a corner reflector, to 1, representing a random mixture of scattering mechanisms
199 (e.g., forest areas).

200 **3. Study area and dataset description**

201 The megafan of Kosi River stretches over 10,300 km² of Northern Bihar plain, India. The fan results from
202 the avulsions and deposition of Himalayan sediments. Based on the movement and pattern of the paleo-
203 channel and modern channels in the Kosi Fan, it is divided into 3 lobes.

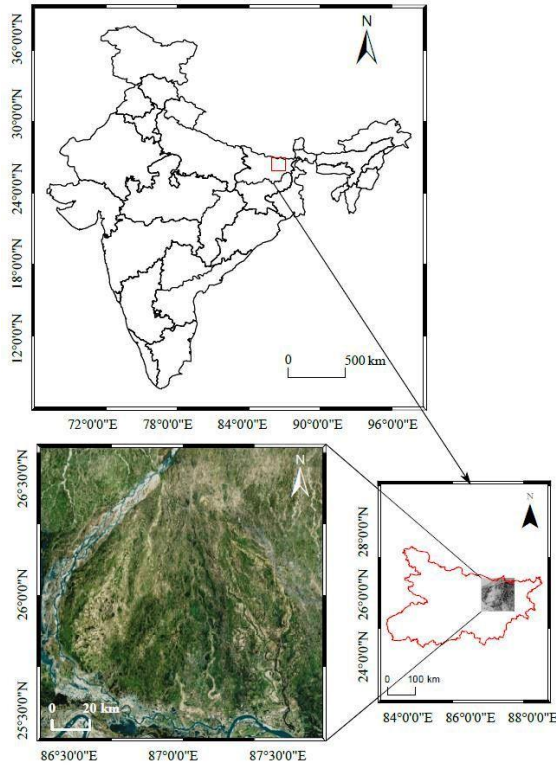


Fig. 1 Study area

204
205
206
207
208
209
210
211
212
213
214

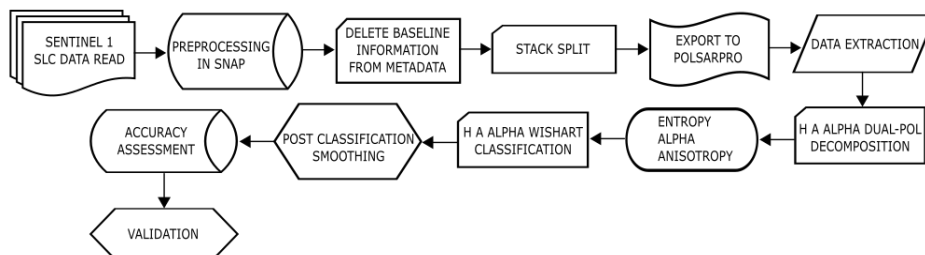
3.1 Sentinel-1A

As the first new space part of the GMES (Global Monitoring for Environment and Security) satellite series, Sentinel-1 is a constellation of two satellites designed and developed by ESA (European Space Agency) and funded by the European Commission. Sentinel-1A carries a C-band SAR instrument (with a 12-day repeat cycle) and has the following four operational modes: Strip map mode (SM), Interferometric Wide Swath mode (IW), Extra Wide Swath mode (EW), and Wave mode (WV). In this study, four tiles of monsoon period Sentinel-1A images were obtained that cover the Kosi megafan. A detailed image information is as below:

Satellite	Year	Date	Polarization	Beam Mode
Sentinel 1A	2017	August	VV+VH	Interferometric Wide(IW)

4. Methodology

All the images were pre-processed in SNAP software, then exported to PolSARPro software for polarimetric processing. The detailed methodology adopted in this study is represented using the following methodology flow diagram:



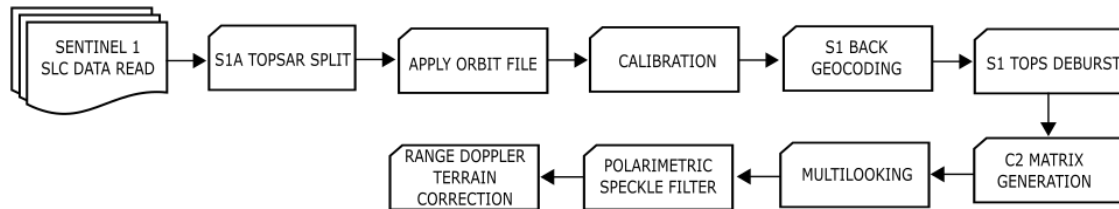
219

220

Fig. 2 Methodology flow chart

221 **4.1 Pre-Processing**

222 The pre-processing of Sentinel-1A data was conducted using SNAP software, including the following
223 process: multi-look, registration, speckle filtering, geocoding, and radiometric calibration. To reduce
224 speckle, a Lee filter with 3×3 windows was applied to all Sentinel-1A images. The Sentinel-1A images
225 were then geocoded using the shuttle radar topography mission DEM with a spatial resolution of 30 m.



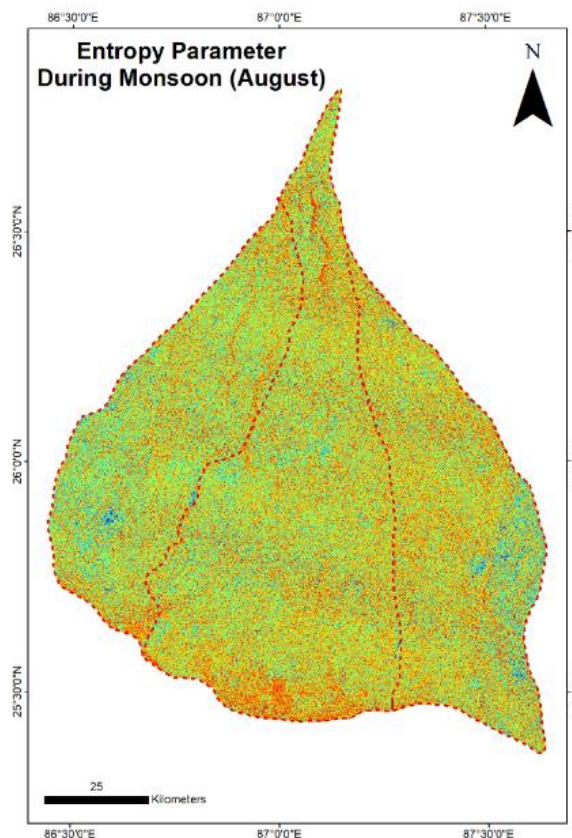
226

227

Fig. 3 Sentinel-1A pre-processing flowchart

228 **5. Results and analysis**

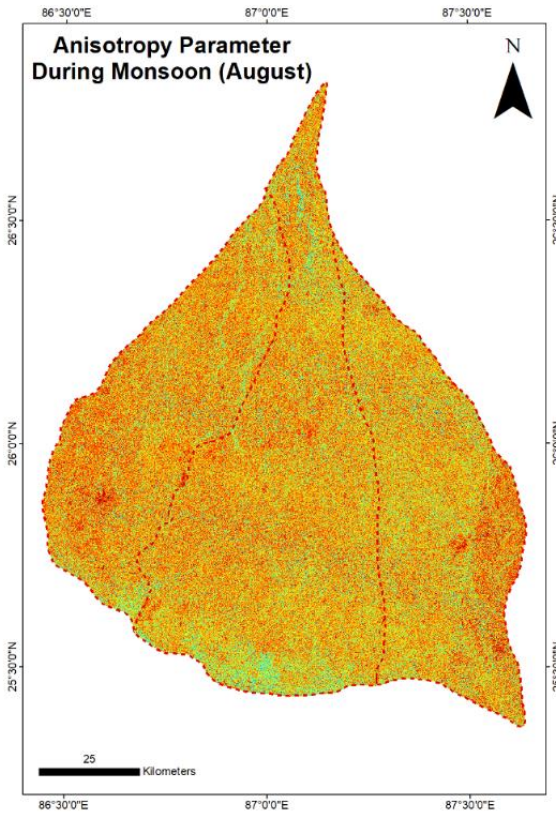
229 The wetlands are clearly classified using Wishart unsupervised H-alpha classification technique. H-A-alpha
230 classifier further improves the classification as it takes anisotropy. The parameters are extracted as per the
231 following figures. H-alpha occurrence plane clearly shows the vegetated wetland with high entropy. Open
232 water areas are also clearly seen in Pauli RGB and also in classified images.



233

234

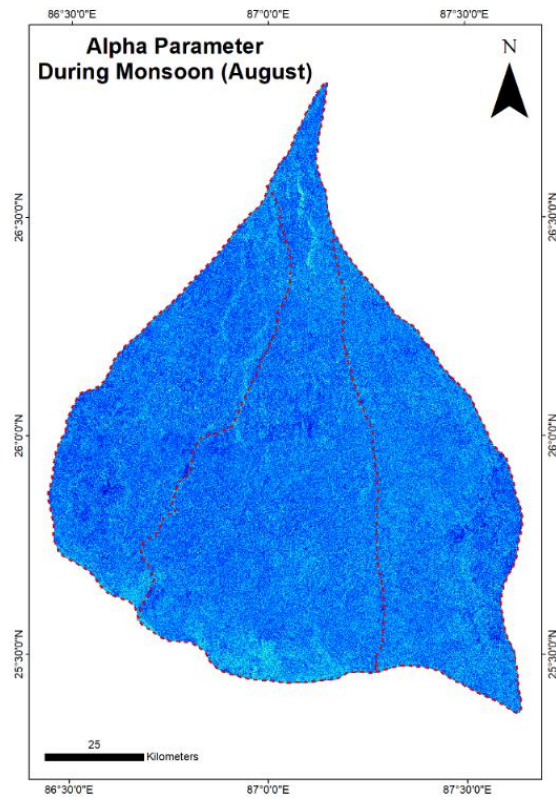
Fig. 4 H-A-Alpha parameter Entropy



235

236

Fig. 5 H-A-Alpha parameter Anisotropy



237

238

Fig. 6 H-A-Alpha parameter Alpha angle

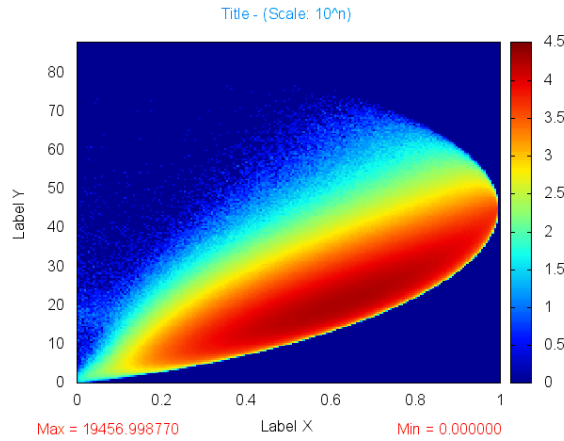
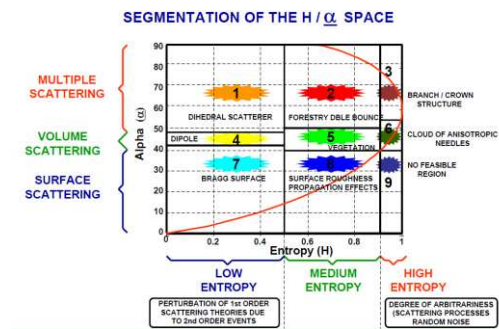


Fig. 7 H-Alpha plane



Source: (Pottier, n.d.)

239 The fig. 8 shows classified map with 16 classes. The class numbers that contribute to different wetland
 240 types are as per following:

- Class 0 = Undefined (neutral)
- Class 1 = High Entropy, Anisotropic, Multiple Scattering
- Class 9 = High Entropy, Isotropic, Multiple Scattering
- Class 10 = High Entropy, Isotropic, Volume Scattering

241

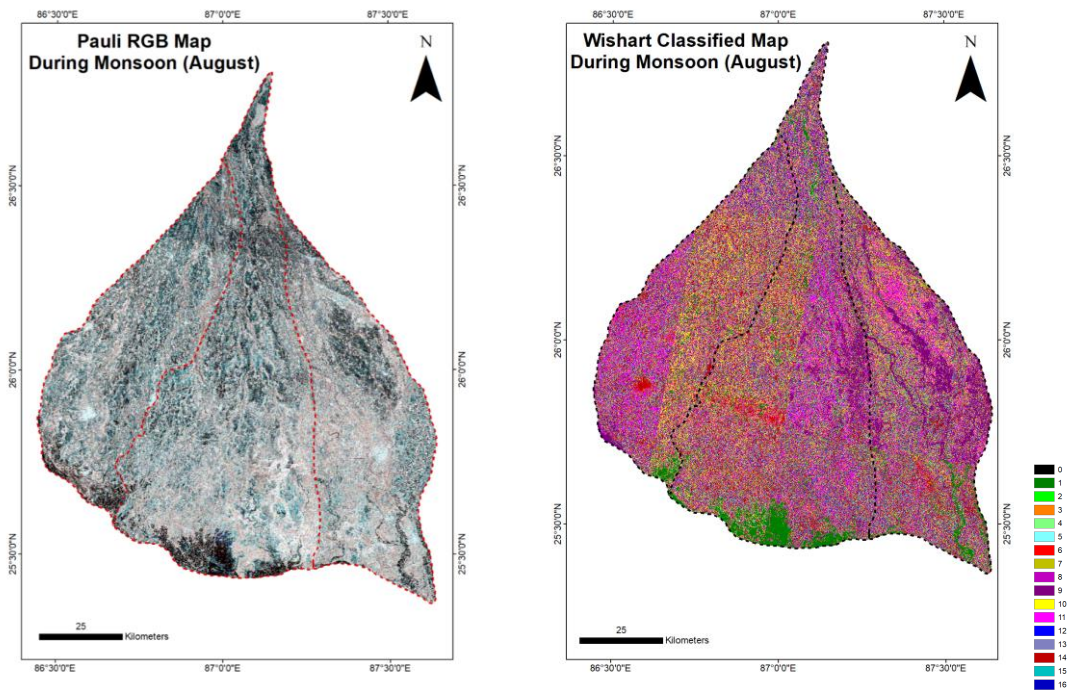
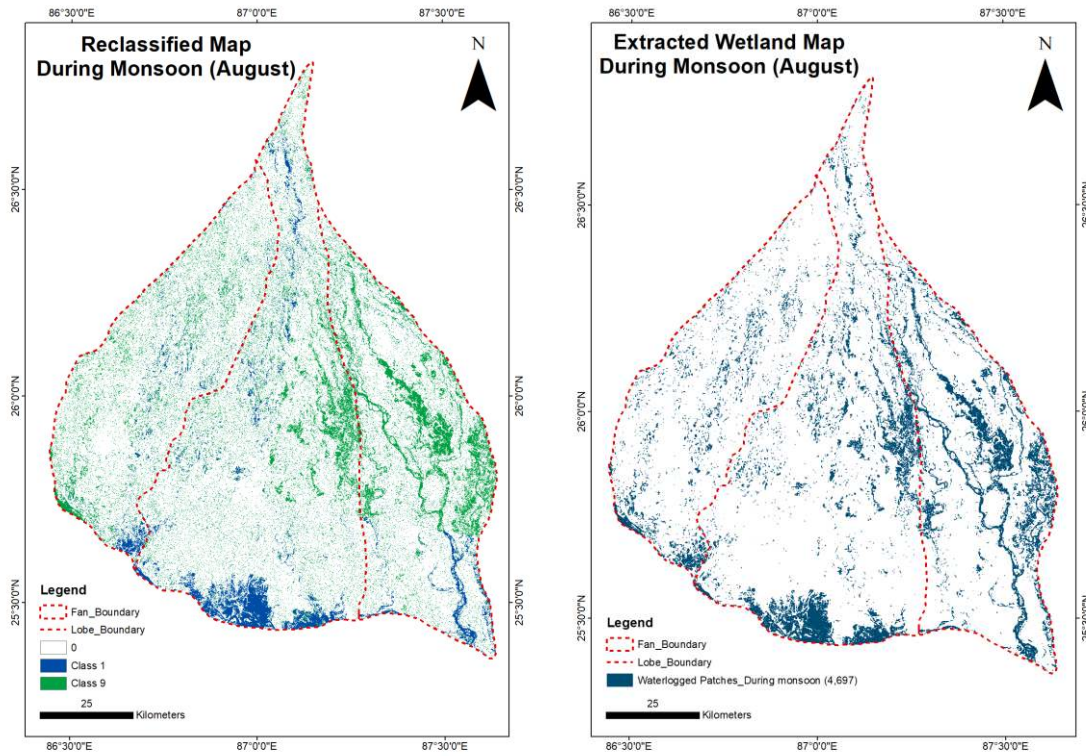


Fig. 8 Decomposed images

242

243 Among the 16 classes it has been observed that class 1, 9 and 10 are showing scattering from wetlands.
 244 These three classes are extracted and processed further in Arcgis software. Some post-classification
 245 smoothing techniques are applied to the polygons. The result shown as per fig. 9. Classification accuracy
 246 is not good due to overlap of backscattering values for vegetation over water and forest land. When we
 247 discard vegetated area in training area selection process, we could classify only open water.



248

Fig. 9 H-A-Alpha classified maps

249

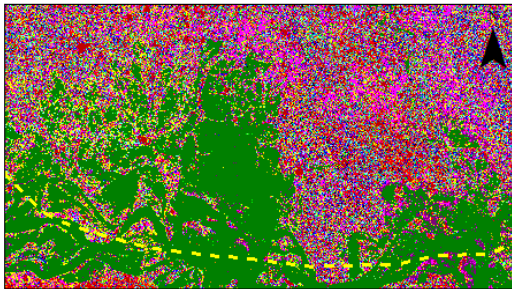
In terms of extraction of the wet soil we experimented with 3X3 and 5X5 window sizes and a greater number of iterations. The results improved and another scattering class 10 with high entropy, isotropic, volume scattering shows periphery of wetlands. The results are shown in fig. 10. The 5X5 window and 50 iterations show best results.

250

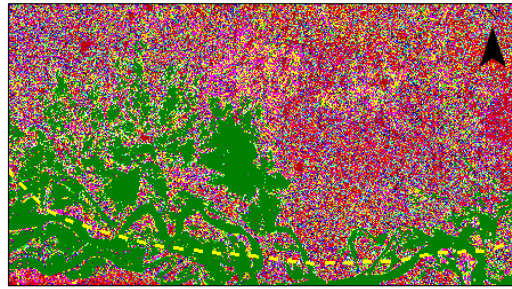
251

252

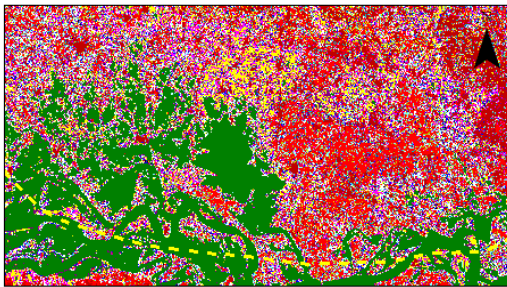
**During monsoon (August 2017)
H-A-Alpha_3X3 Window_10 Iterations**



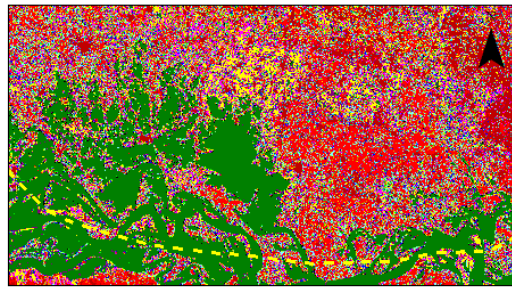
**During monsoon (August 2017)
H-A-Alpha_3X3 Window_50 Iterations**



**During monsoon (August 2017)
H-A-Alpha_5X5 Window_50 Iterations**

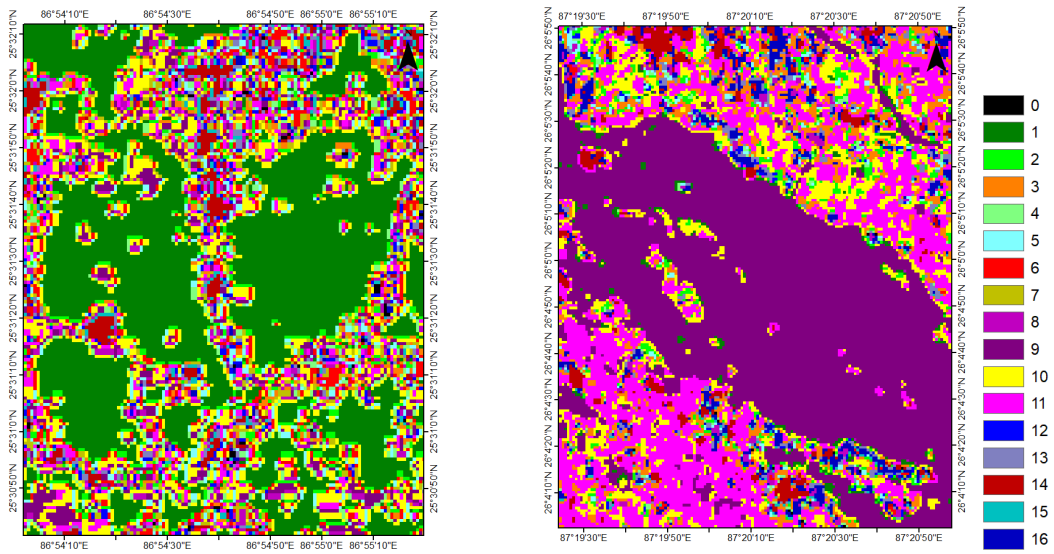


**During monsoon (August 2017)
H-A-Alpha_5X5 Window_100 Iterations**



253

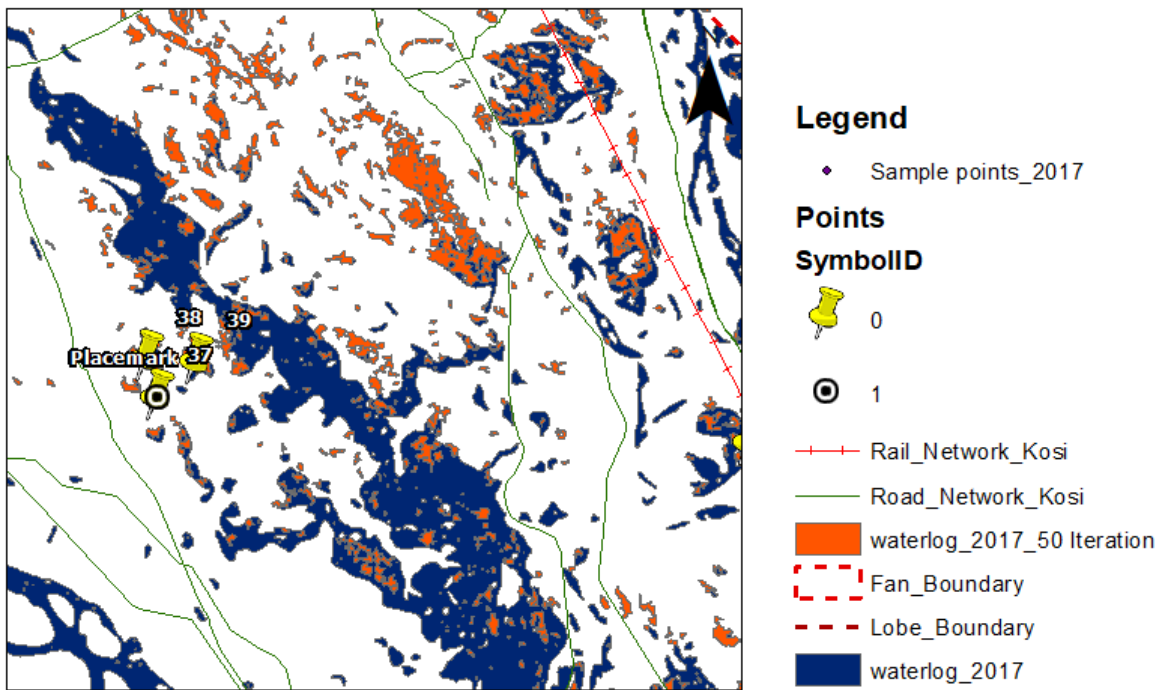
Fig. 10 H-A-Alpha decomposed images with different number of iterations



254

Fig. 11 Final decomposed image showing scattering classes

255

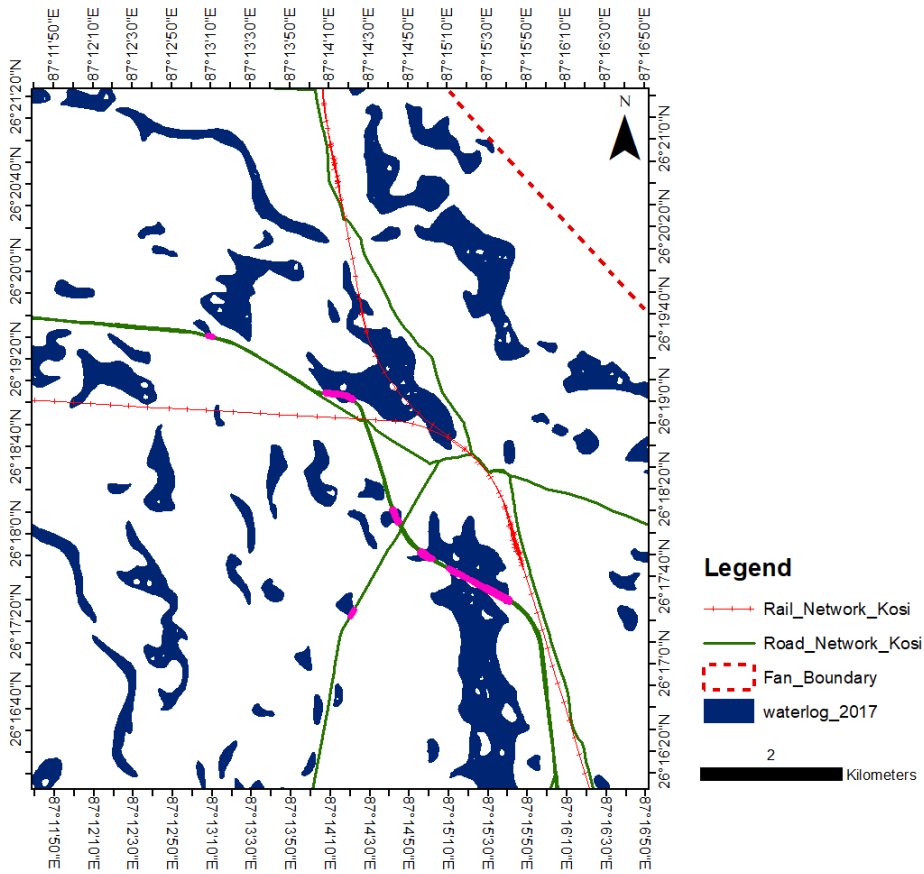


256

Fig. 12 Post-smoothing wetland map

257

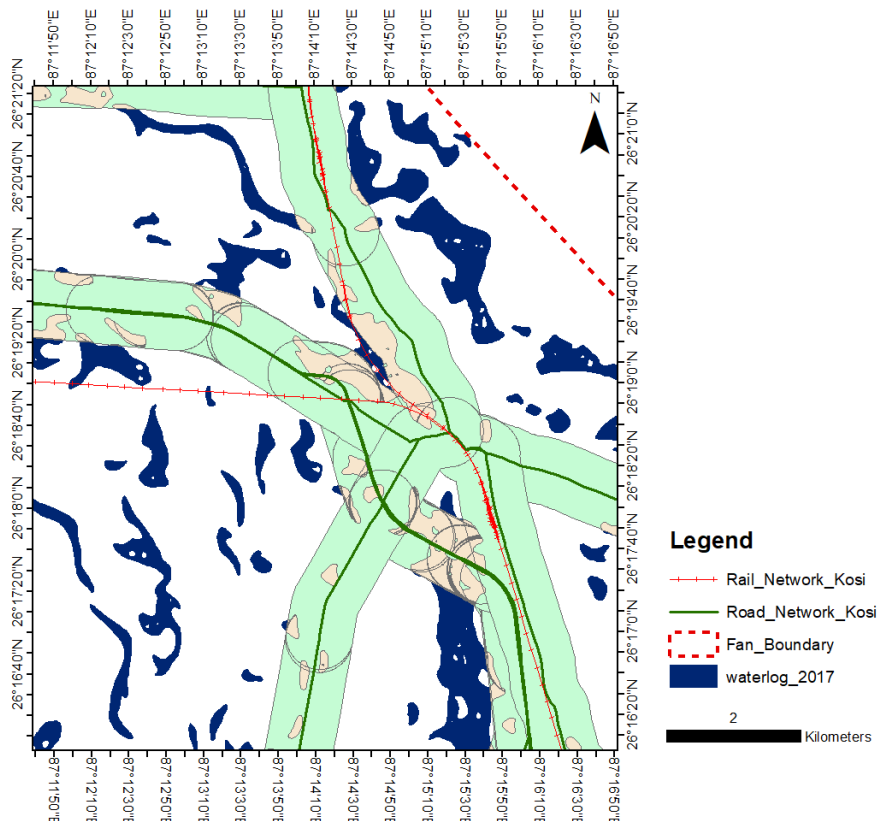
258



259

260

Fig. 13 Waterlogged map with rail-road network intersections

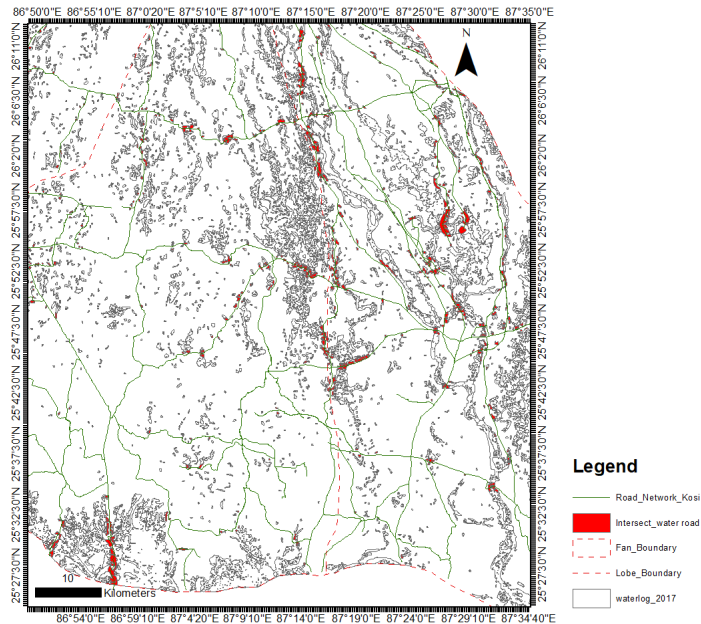


261

262
263
264
265
266
267
268

Fig. 14 Waterlogged map with rail-road network buffer intersections

The extracted wetlands are overlapped with existing rail and road network. Certain areas are zoom in to show the intersecting areas. A 20 m buffer has been taken for major roads. As per fig. it can shown in monsoon period how roads are being waterlogged. In a higher scale the red coloured portions show major intersecting zones with waterlogged roads. Major planning interventions can be drawn further from this study.



269
270

Fig. 15 Waterlogged zones vulnerable to rail-road network

271 6. Discussion

272 The surface of the Kosi Megafan is characterized by low-lying waterbeds. During annual floods water
273 deposits in these low elevated zones. As a result occurrence of marshy land, herbaceous low land is huge
274 which caters more waterlogging during seasons. Many portions of the site is covered with wet alluvial
275 deposits. Vegetation growth over these marshy lands turn into temporary waterlogged patches during and
276 after monsoon. The low lands cater as fishing and aquatic activities, cultivation, small enterprise like brick
277 making etc. the types of wetlands need to be extracted in more efficient way to make use of the land as well
278 as any anthropogenic barriers. The life and livelihoods of communities that are vulnerable to flooding can
279 be marked based on this study.

280 7. Acknowledgements

281 Not applicable.

282 8. Declarations

283 Not applicable.

284 References

- 285 Boerner, Wolfgang-martin. n.d. "Basics of Radar Polarimetry Introduction : A Review of Polarimetry," no. 607.
286 Hong, Sang Hoon, Hyun Ok Kim, Shimon Wdowinski, and Emanuelle Feliciano. 2015. "Evaluation of
287 Polarimetric SAR Decomposition for Classifying Wetland Vegetation Types." *Remote Sensing* 7
288 (7): 8563–85. <https://doi.org/10.3390/rs70708563>.
289 Lee, Jong Sen, Mitchell R. Grunes, Thomas L. Ainsworth, Li Jen Du, Dale L. Schuler, and Shane R.
290 Cloude. 1999. "Unsupervised Classification Using Polarimetric Decomposition and the Complex

291 Wishart Classifier.” *IEEE Transactions on Geoscience and Remote Sensing* 37 (5 pt 1): 2249–58.
 292 <https://doi.org/10.1109/36.789621>.

293 Lee, Jong Sen, and Eric Pottier. 2017. “Polarimetric Radar Imaging: From Basics to Applications.” In
 294 *Polarimetric Radar Imaging: From Basics to Applications*, 1–398. Optical Science and
 295 Engineering. CRC Press. <https://doi.org/10.1201/9781420054989>.

296 Moser, Linda, Andreas Schmitt, Anna Wendleder, and Achim Roth. 2016. *Monitoring of the Lac Bam*
 297 *Wetland Extent Using Dual-Polarized X-Band SAR Data. Remote Sensing*. Vol. 8.
 298 <https://doi.org/10.3390/rs8040302>.

299 Pottier, Eric. n.d. “Polarimetry Basics,” 1–86.

300 Xiang, Deliang. 2016. *Urban Area Information Extraction From Polarimetric SAR Data*.

301 Zhang, Meimei, Zhen Li, Bangsen Tian, Jianmin Zhou, and Panpan Tang. 2016. “The Backscattering
 302 Characteristics of Wetland Vegetation and Water-Level Changes Detection Using Multi-Mode
 303 SAR: A Case Study.” *International Journal of Applied Earth Observation and Geoinformation* 45:
 304 1–13. <https://doi.org/https://doi.org/10.1016/j.jag.2015.10.001>.

305 Zyl, Jakob J. Van, and Yunjin Kim. 2003. “The Use of Polarimetric and Interferometric SAR Data in
 306 Floodplain Mapping.” *International Geoscience and Remote Sensing Symposium (IGARSS) 1*
 307 (August 2003): 443–45. <https://doi.org/10.1109/igarss.2003.1293803>.

308 ZYL, Van. n.d. “Unsupervised Classification of Scattering Behavior Using Radar Polarimetry Data.”

309
 310

LIST OF FIGURES

311 Fig. 1 Study area 7

312 Fig. 2 Methodology flow chart..... 8

313 Fig. 3 Sentinel-1A pre-processing flowchart..... 8

314 Fig. 4 H-A-Alpha parameter Entropy 8

315 Fig. 5 H-A-Alpha parameter Anisotropy..... 9

316 Fig. 6 H-A-Alpha parameter Alpha angle 9

317 Fig. 7 H-Alpha plane 10

318 Fig. 8 Decomposed images..... 10

319 Fig. 9 H-A-Alpha classified maps 11

320 Fig. 10 H-A-Alpha decomposed images with different number of iterations..... 12

321 Fig. 11 Final decomposed image showing scattering classes 12

322 Fig. 12 Post-smoothing wetland map 12

323 Fig. 13 Waterlogged map with rail-road network intersections 13

324 Fig. 14 Waterlogged map with rail-road network buffer intersections..... 14

325 Fig. 15 Waterlogged zones vulnerable to rail-road network..... 14

326

327